ACTA ONCOLOGICA, 2017
VOL. 56, NO. 12, 1754–1762
https://doi.org/10.1080/0284186X.2017.1343494

Taylor & Francis
Taylor & Francis Group

ORIGINAL ARTICLE

Dynamic contrast-enhanced MRI of the microenvironment of pancreatic adenocarcinoma xenografts

Catherine S. Wegner, Anette Hauge, Jon-Vidar Gaustad, Lise Mari K. Andersen, Trude G. Simonsen, Kanthi Galappathi and Einar K. Rofstad

Group of Radiation Biology and Tumor Physiology, Department of Radiation Biology, Institute for Cancer Research, Oslo University Hospital, Oslo, Norway

ABSTRACT

Background: Pancreatic ductal adenocarcinoma (PDAC) is an aggressive disease with poor outcome. Resistance to treatment is associated with impaired vascularity, extensive hypoxia, and interstitial hypertension. In this study, the potential of dynamic contrast-enhanced (DCE)-MRI as a method for assessing the microvascular density (MVD), the fraction of hypoxic tissue, and the interstitial fluid pressure (IFP) of PDACs was investigated.

Material and methods: Intramuscular BxPC-3, Capan-2, MIAPaCa-2, and Panc-1 PDAC xenografts were used as preclinical models of human PDACs. DCE-MRI with Gd-DOTA as contrast agent was conducted with a 7.05-T scanner, and the DCE-MRI series were analyzed voxelwise by using the Tofts pharmacokinetic model. Tumor MVD and hypoxia were measured in histological preparations by using pimonidazole as a hypoxia marker and CD31 as a marker of endothelial cells. IFP was measured with a Millar catheter.

Results: K^{trans} (the volume transfer constant of Gd-DOTA) increased with increasing MVD and decreased with increasing hypoxic fraction, but was not associated with IFP. Any association between v_e (the fractional distribution volume of Gd-DOTA) and MVD, hypoxic fraction, or IFP could not be detected.

Conclusions: This study shows that DCE-MRI is a useful modality for assessing important features of the microenvironment of PDAC xenografts and thus provides the basis for future preclinical and clinical DCE-MRI investigations of PDAC.

ARTICLE HISTORY
Received 2 November 2016
Accepted 10 June 2017

Introduction

Pancreatic ductal adenocarcinoma (PDAC) is the fourth leading cause of cancer-related deaths worldwide [1]. Surgical resection is the only curative treatment option, but most cases are too advanced for surgery at the time of diagnosis. The majority of the patients receive gemcitabin or FOLFIRINOX chemotherapy alone or in combination with radiation therapy [2,3], resulting in a five year survival of only ~6% [1]. Several approaches of targeted treatment have been explored, however, with limited therapeutic effect [4,5].

The low survival rate of PDAC patients is primarily due to resistance to treatment caused by the tumor microenvironment. The microenvironment of PDACs is characterized by a highly desmoplastic stroma encompassing up to 90% of the tumor [3,4], heterogeneous vascularization [6], regions with hypoxic tissue [7], and interstitial hypertension [8]. Treatment strategies targeting the desmoplastic tumor stroma have not been beneficial to PDAC patients thus far [4,9]. Low microvascular density (MVD) and reduced blood flow have been shown to be signs of tumor aggressiveness [10–12], and high MVD in peripheral hot spots has been found to correlate with poor prognosis, suggesting that highly heterogeneous microcirculation aggravates the outcome [6,13]. It has also been revealed that poor prognosis is associated with severe hypoxia in the primary tumor [14–16]. Moreover, the interstitial fluid pressure (IFP) has been reported to be elevated [17–19], and it has been suggested that highly elevated IFP together with a dense and extensive stroma may cause resistance to treatment by inhibiting the distribution of chemotherapeutic agents [19].

Multi-detector computed tomography is the most commonly used imaging modality in the diagnostics of PDAC; however, magnetic resonance imaging (MRI) employing contrast agents has been found to be equally profitable [20]. Although preclinical studies have suggested that dynamic contrast-enhanced (DCE)-MRI may be useful for assessing the therapeutic response of PDAC [21–23], detailed studies comparing DCE-MRI-derived parametric images with parameters of the tumor microenvironment have not been reported thus far. The aim of this study was to evaluate to what extent DCE-MRI can provide information on tumor MVD, hypoxia, and IFP in PDAC xenografts.

CONTACT Catherine Sem Wegner catherine.sem.wegner@rr-research.no Department of Radiation Biology, Institute for Cancer Research, Oslo University Hospital, Box 4953 Nydalen, 0424 Oslo, Norway.

Supplemental data for this article can be accessed here.

Material and methods

Tumor models

BxPC-3, Capan-2, MIAPaCa-2, and Panc-1 human PDAC xenografts grown in adult (8–12 weeks of age) female BALB/c *nu/nu* mice were used as tumor models. Tumors were initiated from cells cultured in RPMI-1640 (25 mM HEPES and L-glutamine) medium supplemented with 13% bovine calf serum, 250 mg/l penicillin, and 50 mg/l streptomycin. Approximately 2.5×10^6 cells in 20–30 µl of Hanks' balanced salt solution were inoculated intramuscularly in the left hind leg. The animal experiments were approved by the Institutional Committee on Research Animal Care and were performed according to the Guidelines for the Welfare and Use of Animals in Cancer Research [24].

Magnetic resonance imaging

MRI was carried out on 12-16 tumors of each model when the tumor volume was judged to be ~700 mm^3 from caliper measurements. The exact tumor volume was determined from the MR images, and the mean values ± standard error were 763 ± 55 mm^3 (BxPC-3), 737 ± 47 mm^3 (Capan-2), 745 ± 50 mm^3 (MIAPaCa-2), and 621 ± 28 mm^3 (Panc-1).

A Bruker Biospec 7.05-T bore magnet and a mouse quadrature volume coil (Bruker Biospin, Ettlingen, Germany) were used for imaging. The tumors were positioned in the isocenter of the magnet and were imaged with axial slices covering the entire volume. The mice were given gas anesthesia (~4.0% Sevofluran in O_2; Baxter, IL, USA) at a flow rate of 0.5 l/min during imaging. Respiration rate and body core temperature were monitored continuously by using an abdominal pressure sensitive probe and a rectal temperature probe (Small Animal Instruments, New York, NY, USA). The body core temperature was kept at 37 °C by automated hot air flow regulation, and the gas anesthesia was adjusted manually to maintain a stable respiration rate.

Anatomical T_2-weighted images were obtained prior to DCE-MRI by using a fast spin echo pulse sequence (RARE) with a repetition time (TR) of 2500 ms, an echo time (TE) of 35 ms, an image matrix of 128×128, a field of view (FOV) of 3×3 cm^2, a slice thickness of 0.7 mm, a slice gap of 0.3 mm, 2 averages, and fat suppression. DCE-MRI with Gd-DOTA (Dotarem, Guerbet, Paris, France) as contrast agent was performed as described elsewhere [25,26]. Briefly, a fast spin echo pulse sequence (RARE) with TRs of 200, 400, 800, 1500, 3000, and 5000 ms, a TE of 8.5 ms, an image matrix of 128×128, a FOV of 3×3 cm^2, a slice thickness of 0.7 mm, and a slice gap of 0.3 mm was applied to measure pre-contrast T_1-values (T_{10}-map). Gd-DOTA was diluted to a concentration of 0.06 M and administered in the tail vein in a bolus dose of 5.0 ml/kg body weight during a period of 5 s by using an automated infusion pump (Harvard Apparatus, Holliston, MA, USA). A three-dimensional SPGR pulse sequence (3D-FLASH) with a TR of 10 ms, a TE of 2.07 ms, a flip angle (α) of 20°, an image matrix of $128 \times 128 \times 10$, and a FOV of $3 \times 3 \times 1$ cm^3 was used to produce dynamic T_1-weighted images at a temporal resolution of 14.8 s.

Numerical values of the volume transfer constant (K^{trans}) and the fractional distribution volume (v_e) of the contrast agent were determined on a voxel-by-voxel basis by using the Tofts pharmacokinetic model [27] as described earlier [25]. Briefly, the pharmacokinetic analysis was based on the entire tumor volume without including peritumoral fibrotic tissue, blood vessels, or edema. Regions of interest (ROIs) encompassing the tumor tissue were depicted in the T_2-weighted anatomical images acquired prior to the DCE-MRI, and these ROIs were transferred to the T_1-weighted images (Figure 1(a)). Parametric images of K^{trans} and v_e were then produced by using in-house-made software developed in Matlab (MathWorks, Natick, MA, USA).

By subjecting tumors and normal muscle tissue to DCE-MRI twice, we have shown that highly reproducible parametric images are obtained by using the imaging and analysis procedures described here (Supplementary Figure S1).

Histological examinations

Sections were cut from three different positions in each tumor and stained with hematoxylin and eosin or immunostained for hypoxia or blood vessels [28]. Pimonidazole [1-[(2-hydroxy-3-piperidinyl)-propyl]-2-nitroimidazole], injected as described previously [29], was used as a marker of tumor hypoxia, and CD31 was used as a marker of endothelial cells. An anti-pimonidazole rabbit polyclonal antibody (Professor Raleigh, University of North Carolina, NC, USA) or an anti-mouse CD31 rabbit polyclonal antibody (Abcam, Cambridge, UK) was used as primary antibody. Diaminobenzidine was used as chromogen, and hematoxylin was used for counterstaining. Microvessels were defined and scored manually as described by Weidner [30]. Fraction of hypoxic tissue was assessed by image analysis [29] and was defined as the area fraction of the viable tissue showing positive pimonidazole staining.

Interstitial fluid pressure

IFP was measured twice in each tumor by using a Millar SPC 320 catheter equipped with a 2F Mikro-Tip transducer (Millar Instruments, Houston, TX, USA). The probe was inserted into the central part of the tumors, first from the lateral side and then from the posterior side. The mean of the two IFP values was utilized in the further analyses. Before measurements, the mice were anesthetized with 0.63 mg/kg fentanyl citrate, 20 mg/kg fluanisone, and 10 mg/kg midazolam. By using these doses and by keeping the body core temperature at 37 °C with a heating pad, it was ensured that tumor blood perfusion and the physiological conditions of the mice during the IFP measurements were similar to those during the MRI [31].

Statistical analysis

Comparisons of data were carried out by using the Student's *t*-test (single comparisons) or by one-way ANOVA followed

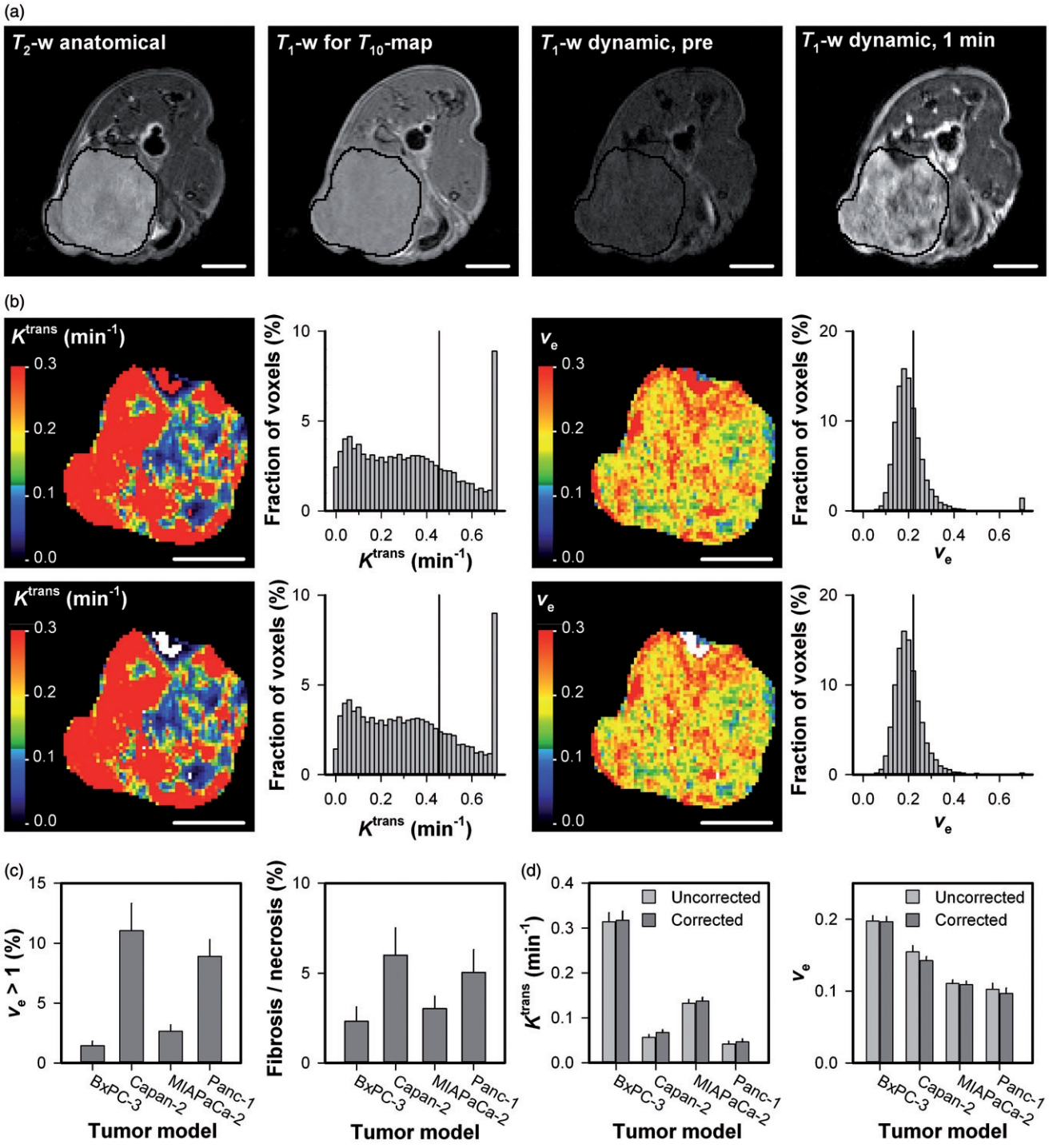

Figure 1. Anatomical and parametric MR images and data of PDAC xenografts. (a) T_2-weighted image, T_1-weighted image acquired for calculation of T_{10}-map, and pre- and post-contrast (recorded 1 min after the administration of Gd-DOTA) T_1-weighted images acquired for calculation of K^{trans} and v_e parametric images. Tumor region of interest (outlined in black in the images) was depicted in the anatomical T_2-weighted image and was transferred directly to the other images since the geometrical setting was the same for the different pulse sequences. The images refer to a representative BxPC-3 tumor. Scale bar: 5 mm. (b) K^{trans} and v_e images and the corresponding K^{trans} and v_e frequency distributions of the same BxPC-3 tumor. The images refer to a central tumor cross-section, whereas the frequency distributions refer to the entire tumor volume. Voxels with unphysiological v_e values (i.e. $v_e > 1.0$) are highlighted in white in the lower panel images, and these voxels are excluded in the corresponding frequency distributions. Median values are indicated by vertical lines in the frequency distributions. Scale bars: 5 mm. (c) Fraction of voxels showing unphysiological v_e values and fraction of tumor tissue showing fibrosis and/or necrosis in BxPC-3, Capan-2, MIAPaCa-2, and Panc-1 tumors. Columns and bars: mean ± SEM [$n = 12$–16 (left panel); $n = 12$–20 (right panel)]. (d) Median K^{trans} and median v_e in BxPC-3, Capan-2, MIAPaCa-2, and Panc-1 tumors. The panels show data where all voxels are included (Uncorrected) and data where voxels with unphysiological v_e values are excluded (Corrected). Columns and bars: mean ± SEM ($n = 12$–16).

by the Bonferroni's test (multiple comparisons) when the data complied with the conditions of normality and equal variance. Under other conditions, comparisons were carried out by non-parametric analysis using the Mann–Whitney rank-sum test (single comparisons) or the Kruskal–Wallis ANOVA on ranks test followed by the Dunn's test (multiple comparisons). The Pearson product moment correlation test was used to search for correlations between parameters.

Probability values of $p < .05$, determined from two-sided tests, were considered significant.

Results

Parametric images of K^{trans} and v_e and the corresponding K^{trans} and v_e frequency distributions of a representative BxPC-3 tumor are presented in Figure 1(b). Supplementary Figure S2 shows similar data for the other three tumor models included in this study. For some voxels, our algorithms produced unphysiological values of v_e (i.e. $v_e > 1.0$), and these voxels are depicted in white in the images and are omitted in the histograms in the lower panels of Figure 1(b) and Supplementary Figure S2. The intratumor heterogeneity in K^{trans} and v_e was substantial in all tumor models. K^{trans} generally showed higher values in the tumor periphery than in central tumor regions, whereas high v_e values were seen both peripherally and centrally. Voxels with unphysiological v_e values tended to co-localize with tumor regions showing fibrotic and/or necrotic tissue. Quantitative studies revealed that the fraction of voxels with unphysiological v_e values was similar to the fraction of tumor tissue showing fibrosis and/or necrosis (Figure 1(c)).

The fraction of voxels with unphysiological v_e values was generally low (Figure 1(c)), and median K^{trans} and v_e were not altered significantly by excluding these voxels (Figure 1(d)). The further analysis was carried out by using the corrected K^{trans} and v_e frequency distributions. The four tumor models differed significantly in K^{trans} and v_e (Figure 1(d)). BxPC-3 showed higher K^{trans} than the other tumor models ($p < .001$), and the K^{trans} of MIAPaCa-2 was higher than that of Capan-2 and Panc-1 ($p < .001$). BxPC-3 also showed higher v_e than the other models ($p < .001$), and the v_e of Capan-2 was higher than that of MIAPaCa-2 and Panc-1 ($p < .001$).

Representative images illustrating the histological appearance of the tumor models are presented in Figure 2. BxPC-3 and Capan-2 showed differentiation, whereas MIAPaCa-2 and Panc-1 were non-differentiated (Figure 2(a)). All tumor

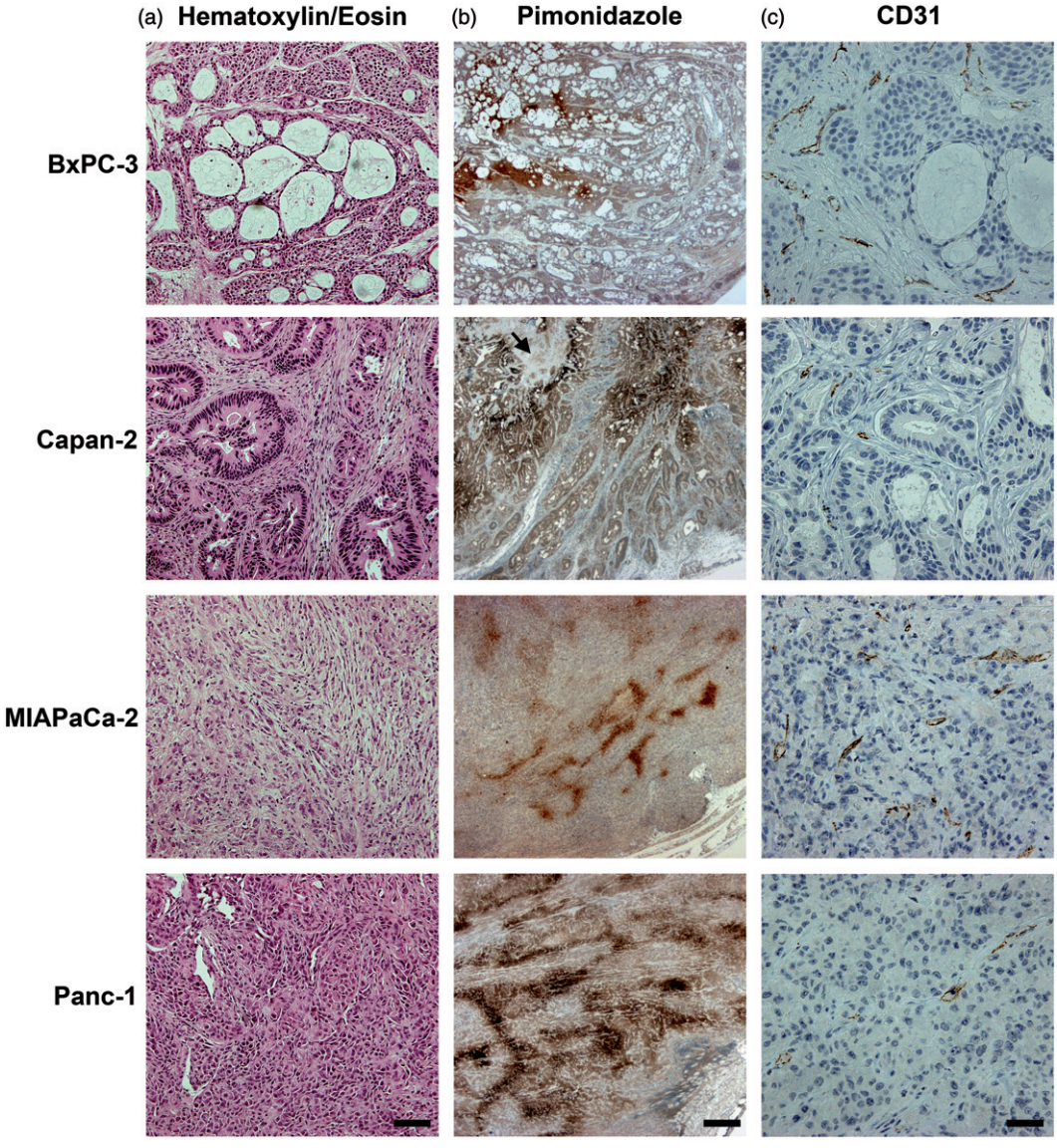

Figure 2. Histological appearance of PDAC xenografts. (a) Preparations stained with hematoxylin and eosin showing the level of differentiation. Scale bar: 200 μm. (b) Preparations immunostained for pimonidazole to visualize tumor hypoxia. Arrow: fibrotic/necrotic tissue. Scale bar: 1000 μm. (c) Preparations immunostained for CD31 to visualize blood vessels. Scale bar: 100 μm.

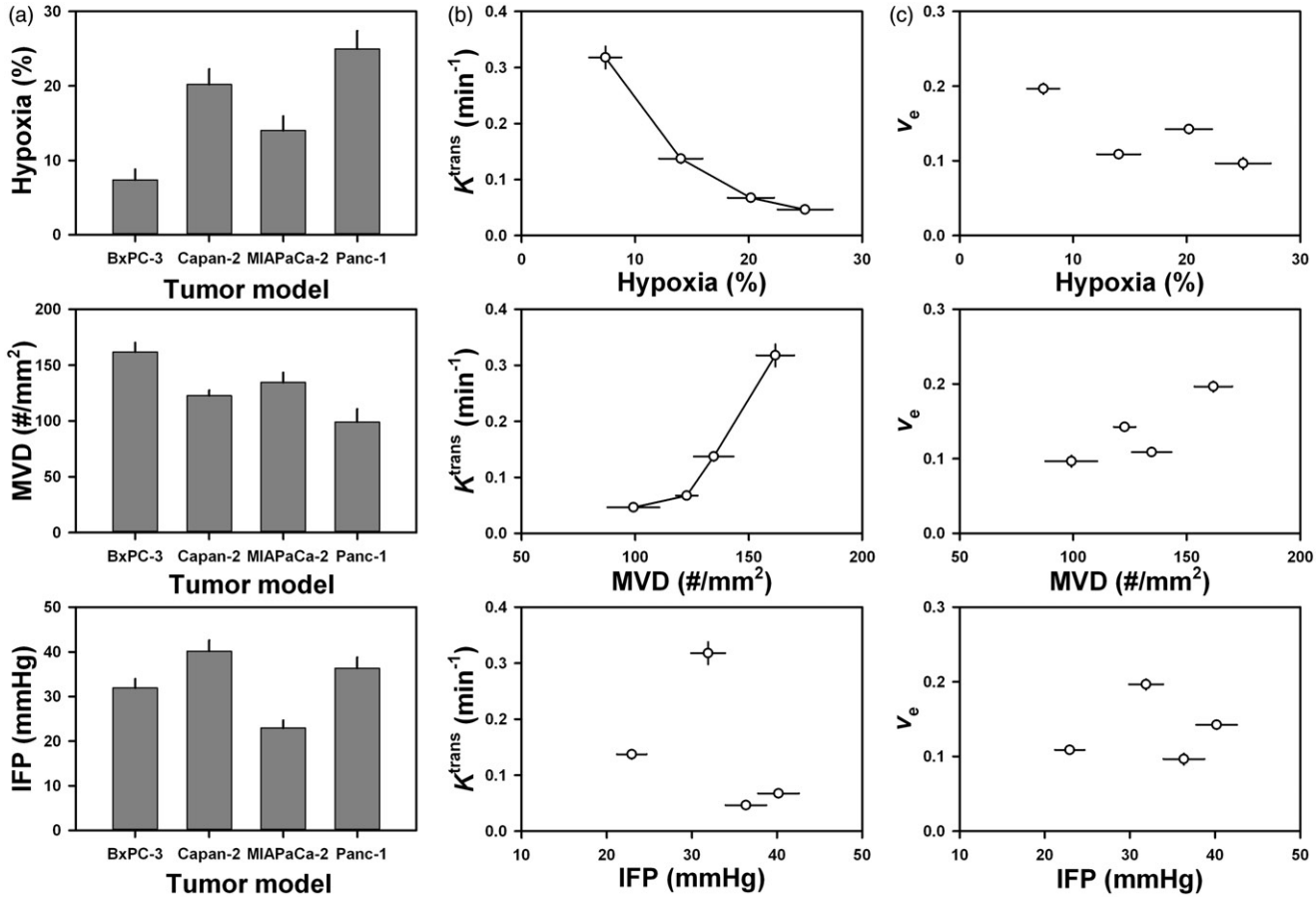

Figure 3. Tumor microenvironment, K^{trans}, and v_e of PDAC xenografts. (a) Fraction of hypoxic tissue, microvascular density (MVD), and interstitial fluid pressure (IFP) in BxPC-3, Capan-2, MIAPaCa-2, and Panc-1 tumors. Columns and bars: mean ± SEM ($n = 12–20$). (b) Median K^{trans} and (c) median v_e versus hypoxic fraction, MVD, and IFP for PDAC xenografts. Points and bars: mean ± SEM [$n = 12–16$ (DCE-MRI parameters); $n = 12–20$ (microenvironmental parameters)]. The DCE-MRI parameters and the microenvironmental parameters were measured in different cohorts of tumor-bearing mice.

models showed foci of pimonidazole-positive cells in morphologically intact tissue, and positive pimonidazole staining was always seen in tissue surrounding fibrotic and necrotic tumor regions (Figure 2(b)). Staining for CD31 showed that blood vessels were located in connective tissue rather than in parenchymal tissue, and this was particularly prominent in BxPC-3 tumors (Figure 2(c)). Quantitative analyses revealed that the fraction of hypoxic tissue and the MVD differed among the tumor models (Figure 3(a)). BxPC-3 showed lower hypoxic fraction ($p < .01$) and higher MVD ($p < .05$) than the other tumor models, and MIAPaCa-2 had lower hypoxic fraction than Capan-2 and Panc-1 ($p < .05$) and higher MVD than Panc-1 ($p < .05$).

All tumor models showed highly elevated IFP. Mean IFP differed among the models from 22.9 mmHg to 40.2 mmHg (Figure 3(a)), and these values were significantly higher than the mean IFP of 0.8 mmHg measured in muscle tissue without tumors ($p < .001$). Moreover, the IFP was lower in MIAPaCa-2 than in the other tumor models ($p < .005$), and BxPC-3 showed lower IFP than Capan-2 ($p < .01$).

To investigate whether DCE-MRI may have the potential to provide information on the tumor microenvironment of PDACs, mean of median K^{trans} and mean of median v_e were plotted *versus* mean fraction of hypoxic tissue, mean MVD, and mean IFP. K^{trans} decreased with increasing hypoxic fraction and increased with increasing MVD, whereas there was no correlation between K^{trans} and IFP (Figure 3(b)). Furthermore, there was no correlation between v_e and hypoxic fraction, MVD, or IFP; however, v_e tended to decrease with increasing hypoxic fraction and to increase with increasing MVD (Figure 3(c)).

The differences in K^{trans}, v_e, hypoxic fraction, and MVD between the individual tumors of each model were small compared with the differences between the models. To investigate whether DCE-MRI may be sufficiently sensitive to detect microenvironmental differences between individual tumors of the same model, DCE-MRI was carried out on 12 BxPC-3 tumors before the hypoxic fraction and MVD of the tumors were measured in histological preparations. K^{trans} decreased with increasing hypoxic fraction and increased with increasing MVD also in this experiment ($p < .001$; Figure 4(a)), and moreover, there was no correlation between v_e and hypoxic fraction or MVD ($p > .05$; Figure 4(b)).

Discussion

Several preclinical models are currently being used in studies of PDAC, including genetically engineered mouse (GEM) models, ectopic or orthotopic patient-derived xenograft models, and subcutaneous cell line-derived xenograft models [32]. GEM models have the advantage that the tumors arise spontaneously in the pancreas of immune-competent mice,

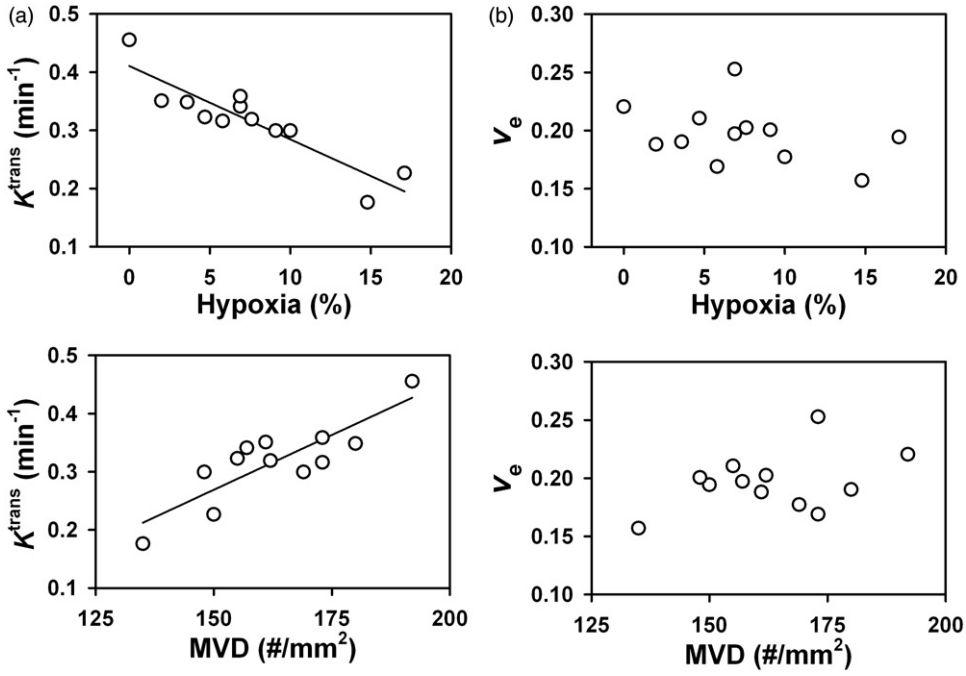

Figure 4. K^{trans}, v_e, and microenvironmental parameters of BxPC-3 PDAC xenografts. Median K^{trans} (a) and median v_e (b) *versus* fraction of hypoxic tissue and microvascular density (MVD). Points: single tumors. Curves: linear regression lines.

allowing studies of the interaction between the tumor microenvironment, the pancreas, and an intact immune system [33]. The main disadvantages of GEM models are that the tumor cells are of murine origin and that the intertumor heterogeneity is low compared with that of human PDACs. Xenograft models have the advantage that the tumors consist of human malignant cells, and furthermore, by using a panel of models derived from different patients, patient-relevant intertumor heterogeneity can be achieved. Four intramuscular cell line-derived xenograft models differing in differentiation were used in the present DCE-MRI study. The tumors were transplanted to an intramuscular site on the mouse leg to avoid tissue movement due to respiration during the MRI.

These tumor models have several microenvironmental features in common with GEM models of PDAC and human PDACs. The tumors develop a dense collagen-rich extracellular matrix [26], consistent with the observation that collagen I is up-regulated in human PDAC [34]. In BxPC-3 and Capan-2 tumors, the collagen fibers appear in thick filament bundles, whereas in MIAPaCa-2 and Panc-1 tumors, the collagen is seen as a dense network of thin fibers surrounding single tumor cells [26]. The tumor microvessels are embedded in the connective tissue as seen in GEM PDAC models [35]. Quantitative studies have revealed that human PDACs may differ considerably in MVD and that the MVD can approximate that of the normal pancreas in some patients [11,36]. The mean MVD of the tumor models included in our study ranged from 99 to 162 (#/mm^2), which is similar to the range of 88–177 (#/mm^2) found in a comprehensive study involving 52 PDAC patients [37].

Studies of IFP and hypoxia in human PDAC are sparse; however, a small study involving seven patients showed that the pO_2 is significantly reduced compared with that in the normal pancreas [7]. The mean fraction of hypoxic tissue in the PDAC models studied here ranged from 7% to 25%, which is similar to the range of 0–25% measured in an extensive study involving orthotopic patient-derived xenograft models from 16 PDAC patients [14]. Furthermore, our PDAC models showed mean IFP values ranging from 23 to 40 mmHg, and these values are similar to those measured in other intramuscular tumor models [38] and in some GEM models of PDAC [17], but lower than those of 75–130 mmHg measured in other GEM PDAC models [8]. It should be noted, however, that the validity of the high IFP values reported by Provenzano *et al.* [8] has been questioned by Chauhan *et al.* [17].

The DCE-MRI data were analyzed by applying the Tofts pharmacokinetic model [27]. This model is based on several assumptions that have been described in detail by Tofts *et al.* [27]. We have shown that the Tofts model gives good fits to Gd-DOTA concentration-versus-time curves for single voxels in the viable tissue of the PDAC models studied here [26], suggesting that the assumptions of the model are adequately fulfilled in vascularized PDAC tissue. However, the model breaks down in poorly and non-vascularized tumor regions, and when it breaks down, our algorithms produce unphysiologically high values for v_e, often higher than 1000 [39]. The present study revealed that voxels in tumor regions with fibrotic and/or necrotic tissue showed unphysiological v_e values and that the fraction of voxels with $v_e > 1.0$ was associated with the fraction of fibrotic and/or necrotic tissue. Because the fraction of voxels with unphysiological v_e values was relatively low (usually $<15\%$), the median values of the K^{trans} and v_e frequency distributions were not changed significantly by excluding these voxels, suggesting that it may

not be necessary to correct for fibrotic and necrotic tissue when calculating the median K^{trans} and median v_e of PDACs.

The BxPC-3, Capan-2, MIAPaCa-2, and Panc-1 cell lines were established from four different PDAC patients, and consequently, the xenografted tumors initiated from these cell lines are preclinical models of four human PDACs. Most likely, the microenvironmental differences between these models are caused primarily by genetic differences between their tumor cells. The individual tumors of each model also developed different microenvironments, although they were initiated from the same cell suspension and thus should be genetically similar. The differences between the microenvironments of these tumors were probably a consequence of stochastic processes involved in the initiation of tumor angiogenesis. K^{trans} increased with increasing MVD and decreased with increasing hypoxia, both when the different models were considered and when the individual tumors of the BxPC-3 model were examined. These data suggest that DCE-MRI may be a useful imaging modality for assessing vascular density and extent of hypoxia in PDAC.

On the other hand, neither K^{trans} nor v_e correlated with IFP in this study, an observation that is consistent with studies having revealed that the IFP of tumors does not correlate with tumor oxygen tension [40,41] and the suggestion that tumor IFP is independent of the extent of tumor hypoxia [38]. Although weak correlations between K^{trans}- and v_e-related MR parameters and IFP have been reported for some melanoma xenograft models [31], other MR parameters may be more appropriate for non-invasive assessment of the IFP of PDACs. The outward peritumoral fluid flow velocity at the tumor surface (v_0) is an interesting MR parameter in that respect, because significant correlations have been found between v_0 and IFP in cervix carcinoma xenografts [42] and between v_0 and outcome of treatment in locally advanced carcinoma of the uterine cervix [43].

The potential of DCE-MRI as a non-invasive method for assessing the fraction of hypoxic tissue in tumors has been studied extensively in our group by using melanoma and cervix carcinoma xenografts as preclinical models of human cancer [39,44,45]. These studies showed that K^{trans} is a stronger predictor of tumor hypoxia than v_e, similar to what was observed for PDAC xenografts in the present study. Moreover, the shape of the plot of K^{trans} versus hypoxic fraction reported here for PDAC xenografts is qualitatively similar to that reported for the melanoma and cervix carcinoma xenografts [39,44]. In all three tumor types, the K^{trans}-versus-hypoxic-fraction curve was steep in the low-hypoxia range and flattened out at larger hypoxic fractions, suggesting that K^{trans} may have larger power to discriminate between tumors differing in hypoxic fraction in the low-hypoxia range than in the high-hypoxia range.

These MR similarities are also interesting because the melanoma, cervix carcinoma, and PDAC xenografts differed considerably in histological appearance [26,46–49]. The PDAC and cervix carcinoma xenografts both developed substantial stroma, but the connective tissue was more extensive and the density of collagen fibers was higher in the PDAC than in the cervix carcinoma xenografts. Furthermore, many blood vessels were located within the connective tissue rather than in the tumor parenchyma, a feature that was not so pronounced in the cervix carcinoma xenografts as in the PDAC xenografts. The melanoma xenografts showed a sparse stroma with little collagen, and the majority of the blood vessels were not separated from the tumor parenchyma by connective tissue. A dense extracellular matrix of collagen and other proteins may limit the transvascular and interstitial transport of MR contrast agents in tumors [50,51]. The similarity of the present observations on PDAC xenografts and our previous findings on melanoma and cervix carcinoma xenografts suggests that the barrier to the transport of Gd-DOTA in PDAC xenografts is not so substantial that the assumptions of the Tofts model are not adequately fulfilled. The associations between K^{trans} and fraction of hypoxic tissue may thus be qualitatively similar for tumor types differing significantly in stromal content and extracellular matrix density and, if so, the interpretation of K^{trans} images in clinical DCE-MRI of malignant tissues will be less demanding.

MRI is currently being used in attempts to detect malignant tissue in the pancreas at an early stage and to provide anatomical information on advanced PDACs [20]. This preclinical study suggests that DCE-MRI may have the potential to provide microenvironmental information on PDACs in addition to anatomical information, particularly information on tumor hypoxia. If our observations can be verified in clinical investigations, DCE-MRI could be used to monitor changes in tumor oxygenation induced by therapeutic interventions (e.g. antiangiogenic treatment), select patients for radiation therapy trials involving hypoxia modifications, and guide personalized treatment of PDAC. Consequently, the potential of DCE-MRI as a non-invasive imaging modality for assessing the oxygenation status of PDACs merits to be evaluated thoroughly in clinical investigations.

Some small clinical studies investigating the potential of quantitative DCE-MRI in the diagnostics of PDAC have been reported recently [52–54]. The K^{trans} values of the primary tumors were found to be lower than those of the adjacent normal pancreatic parenchyma in all studies, but even though all analyses were conducted by using the two-compartment pharmacokinetic model of Tofts, the mean K^{trans} value of the PDACs differed among the studies by a factor of ~240. Although some of this variability can be attributed to methodological differences such as differences in image acquisition parameters and the use of different contrast agents, these studies illustrate that quantitative DCE-MRI of PDAC is challenging. Several problems were identified, including the assessment of an adequate arterial input function and accurate tumor delineation [52–54]. The most serious problem is probably tumor motion during the DCE-MRI [52]. Tumor motion is caused by patient breathing and movement of abdominal organs and complicates voxel-by-voxel analysis of DCE-MRI series. Adequate solutions to these problems are required and standardized DCE-MRI protocols need to be established before reproducible DCE-MRI-derived parametric images of PDACs can be produced.

In summary, K^{trans} was found to increase with increasing MVD and to decrease with increasing fraction of hypoxic tissue in PDAC xenografts, whereas a significant correlation between K^{trans} and IFP could not be detected.

The association between K^{trans} and fraction of hypoxic tissue was qualitatively similar to those we have reported previously for melanoma and cervix carcinoma xenografts. Taken together, our data show that K^{trans} may have the power to assess the extent of hypoxia in tumors, and furthermore, they suggest that DCE-MRI may be a clinically useful imaging modality for assessing the hypoxic fraction of tumors regardless of the extent and density of the extracellular matrix.

Acknowledgments

We thank the MRI Core Facility for Preclinical Cancer Research at the Norwegian Radium Hospital for the use of the Bruker Biospec 7-T MR scanner and the Norwegian Cancer Society and the South-Eastern Norway Regional Health Authority for financial support.

Disclosure statement

The authors have no conflicts of interest.

Funding

Norwegian Cancer Society and South-Eastern Norway Regional Health Authority.

References

[1] Rahib L, Smith BD, Aizenberg R, et al. Projecting cancer incidence and deaths to 2030: the unexpected burden of thyroid, liver, and pancreas cancers in the United States. Cancer Res. 2014;74:2913–2921.

[2] Boyle J, Czito B, Willett C, et al. Adjuvant radiation therapy for pancreatic cancer: a review of the old and the new. J Gastrointest Oncol. 2015;6:436–444.

[3] Neesse A, Algul H, Tuveson DA, et al. Stromal biology and therapy in pancreatic cancer: a changing paradigm. Gut 2015;64:1476–1484.

[4] Di Marco M, Grassi E, Durante S, et al. State of the art biological therapies in pancreatic cancer. World J Gastrointest Oncol. 2016;8:55–66.

[5] Moore MJ, Goldstein D, Hamm J, et al. Erlotinib plus gemcitabine compared with gemcitabine alone in patients with advanced pancreatic cancer: a phase III trial of the national cancer institute of Canada clinical trials group. J Clin Oncol. 2007;25:1960–1966.

[6] Ikeda N, Adachi M, Taki T, et al. Prognostic significance of angiogenesis in human pancreatic cancer. Br J Cancer. 1999;79:1553–1563.

[7] Koong AC, Mehta VK, Le QT, et al. Pancreatic tumors show high levels of hypoxia. Int J Radiat Oncol Biol Phys. 2000;48:919–922.

[8] Provenzano PP, Cuevas C, Chang AE, et al. Enzymatic targeting of the stroma ablates physical barriers to treatment of pancreatic ductal adenocarcinoma. Cancer Cell. 2012; 21:418–429.

[9] Ozdemir BC, Pentcheva-Hoang T, Carstens JL, et al. Depletion of carcinoma-associated fibroblasts and fibrosis induces immunosuppression and accelerates pancreas cancer with reduced survival. Cancer Cell. 2014;25:719–734.

[10] Barau A, Ruiz-Sauri A, Valencia G, et al. High microvessel density in pancreatic ductal adenocarcinoma is associated with high grade. Virchows Arch. 2013;462:541–546.

[11] Di Maggio F, Arumugam P, Delvecchio FR, et al. Pancreatic stellate cells regulate blood vessel density in the stroma of pancreatic ductal adenocarcinoma. Pancreatology. 2016;16:995–1004.

[12] Komar G, Kauhanen S, Liukko K, et al. Decreased blood flow with increased metabolic activity: a novel sign of pancreatic tumor aggressiveness. Clin Cancer Res. 2009;15:5511–5517.

[13] Karademir S, Sokmen S, Terzi C, et al. Tumor angiogenesis as a prognostic predictor in pancreatic cancer. J Hepatobiliary Pancreat Surg. 2000;7:489–495.

[14] Chang Q, Jurisica I, Do T, et al. Hypoxia predicts aggressive growth and spontaneous metastasis formation from orthotopically grown primary xenografts of human pancreatic cancer. Cancer Res. 2011;71:3110–3120.

[15] Ide T, Kitajima Y, Miyoshi A, et al. The hypoxic environment in tumor-stromal cells accelerates pancreatic cancer progression via the activation of paracrine hepatocyte growth factor/c-met signaling. Ann Surg Oncol. 2007;14:2600–2607.

[16] Miller BW, Morton JP, Pinese M, et al. Targeting the LOX/hypoxia axis reverses many of the features that make pancreatic cancer deadly: inhibition of LOX abrogates metastasis and enhances drug efficacy. EMBO Mol Med. 2015;7:1063–1076.

[17] Chauhan VP, Boucher Y, Ferrone CR, et al. Compression of pancreatic tumor blood vessels by hyaluronan is caused by solid stress and not interstitial fluid pressure. Cancer Cell. 2014;26:14–15.

[18] DuFort CC, DelGiorno KE, Carlson MA, et al. Interstitial pressure in pancreatic ductal adenocarcinoma is dominated by a gel-fluid phase. Biophys J. 2016;110:2106–2119.

[19] Provenzano PP, Hingorani SR. Hyaluronan, fluid pressure, and stromal resistance in pancreas cancer. Br J Cancer. 2013;108:1–8.

[20] Pietryga JA, Morgan DE. Imaging preoperatively for pancreatic adenocarcinoma. J Gastrointest Oncol. 2015;6:343–357.

[21] Cardenas-Rodriguez J, Li Y, Galons JP, et al. Imaging biomarkers to monitor response to the hypoxia-activated prodrug TH-302 in the MiaPaCa2 flank xenograft model. Magn Reson Imaging. 2012;30:1002–1009.

[22] Cham KK, Baker JH, Takhar KS, et al. Metronomic gemcitabine suppresses tumour growth, improves perfusion, and reduces hypoxia in human pancreatic ductal adenocarcinoma. Br J Cancer. 2010;103:52–60.

[23] Zhang X, Wojtkowiak JW, Martinez GV, et al. MR imaging biomarkers to monitor early response to hypoxia-activated prodrug TH-302 in pancreatic cancer xenografts. PLoS One. 2016;11:e0155289.

[24] Workman P, Aboagye EO, Balkwill F, et al. Guidelines for the welfare and use of animals in cancer research. Br J Cancer. 2010;102:1555–1577.

[25] Gaustad JV, Simonsen TG, Smistad R, et al. Early effects of low dose bevacizumab treatment assessed by magnetic resonance imaging. BMC Cancer. 2015;15:900.

[26] Wegner CS, Gaustad JV, Andersen LM, et al. Diffusion-weighted and dynamic contrast-enhanced MRI of pancreatic adenocarcinoma xenografts: associations with tumor differentiation and collagen content. J Transl Med. 2016;14:161.

[27] Tofts PS, Brix G, Buckley DL, et al. Estimating kinetic parameters from dynamic contrast-enhanced T_1-weighted MRI of a diffusable tracer: standardized quantities and symbols. J Magn Reson Imaging. 1999;10:223–232.

[28] Rofstad EK, Måseide K. Radiobiological and immunohistochemical assessment of hypoxia in human melanoma xenografts: acute and chronic hypoxia in individual tumours. Int J Radiat Biol. 1999;75:1377–1393.

[29] Rofstad EK, Galappathi K, Mathiesen B, et al. Fluctuating and diffusion-limited hypoxia in hypoxia-induced metastasis. Clin Cancer Res. 2007;13:1971–1978.

[30] Weidner N. Intratumor microvessel density as a prognostic factor in cancer. Am J Pathol. 1995;147:9–19.

[31] Gulliksrud K, Brurberg KG, Rofstad EK. Dynamic contrast-enhanced magnetic resonance imaging of tumor interstitial fluid pressure. Radiother Oncol. 2009;91:107–113.

[32] Richmond A, Su YJ. Mouse xenograft models *vs* GEM models for human cancer therapeutics. Dis Model Mech. 2008;1:78–82.

[33] Qiu W, Su GH. Challenges and advances in mouse modeling for human pancreatic tumorigenesis and metastasis. Cancer Metast Rev. 2013;32:83–107.

[34] Grzesiak JJ, Ho JC, Moossa AR, et al. The integrin-extracellular matrix axis in pancreatic cancer. Pancreas 2007;35:293–301.
[35] Olive KP, Jacobetz MA, Davidson CJ, et al. Inhibition of hedgehog signaling enhances delivery of chemotherapy in a mouse model of pancreatic cancer. Science 2009;324:1457–1461.
[36] Rhim AD, Oberstein PE, Thomas DH, et al. Stromal elements act to restrain, rather than support, pancreatic ductal adenocarcinoma. Cancer Cell. 2014;25:735–747.
[37] Hoem D, Straume O, Immervoll H, et al. Vascular proliferation is associated with survival in pancreatic ductal adenocarcinoma. APMIS. 2013;121:1037–1046.
[38] Lunt SJ, Kalliomaki TM, Brown A, et al. Interstitial fluid pressure, vascularity and metastasis in ectopic, orthotopic and spontaneous tumours. BMC Cancer. 2008;8:2.
[39] Egeland TA, Gulliksrud K, Gaustad JV, et al. Dynamic contrast-enhanced-MRI of tumor hypoxia. Magn Reson Med. 2012;67:519–530.
[40] Boucher Y, Lee I, Jain RK. Lack of general correlation between interstitial fluid pressure and oxygen partial pressure in solid tumors. Microvasc Res. 1995;50:175–182.
[41] Fyles A, Milosevic M, Pintilie M, et al. Long-term performance of interstial fluid pressure and hypoxia as prognostic factors in cervix cancer. Radiother Oncol. 2006; 80:132–137.
[42] Hompland T, Ellingsen C, Øvrebø KM, et al. Interstitial fluid pressure and associated lymph node metastasis revealed in tumors by dynamic contrast-enhanced MRI. Cancer Res. 2012;72: 4899–4908.
[43] Hompland T, Lund KV, Ellingsen C, et al. Peritumoral interstitial fluid flow velocity predicts survival in cervical carcinoma. Radiother Oncol. 2014;113:132–138.
[44] Ellingsen C, Egeland TA, Gulliksrud K, et al. Assessment of hypoxia in human cervical carcinoma xenografts by dynamic contrast-enhanced magnetic resonance imaging. Int J Radiat Oncol Biol Phys. 2009;73:838–845.
[45] Gulliksrud K, Øvrebø KM, Mathiesen B, et al. Differentiation between hypoxic and non-hypoxic experimental tumors by dynamic contrast-enhanced magnetic resonance imaging. Radiother Oncol. 2011;98:360–364.
[46] Ellingsen C, Egeland TA, Galappathi K, et al. Dynamic contrast-enhanced magnetic resonance imaging of human cervical carcinoma xenografts: pharmacokinetic analysis and correlation to tumor histomorphology. Radiother Oncol. 2010;97:217–224.
[47] Ellingsen C, Hompland T, Galappathi K, et al. DCE-MRI of the hypoxic fraction, radioresponsiveness, and metastatic propensity of cervical carcinoma xenografts. Radiother Oncol. 2014;110: 335–341.
[48] Ellingsen C, Øvrebø KM, Galappathi K, et al. pO_2 fluctuation pattern and cycling hypoxia in human cervical carcinoma and melanoma xenografts. Int J Radiat Oncol Biol Phys. 2012;83:1317–1323.
[49] Rofstad EK, Mathiesen B. Metastasis in melanoma xenografts is associated with tumor microvascular density rather than extent of hypoxia. Neoplasia 2010;12:889–898.
[50] Chauhan VP, Stylianopoulos T, Boucher Y, et al. Delivery of molecular and nanoscale medicine to tumors: transport barriers and strategies. Annu Rev Chem Biomol Eng. 2011;2:281–298.
[51] Netti PA, Berk DA, Swartz MA, et al. Role of extracellular matrix assembly in interstitial transport in solid tumors. Cancer Res. 2000;60:2497–2503.
[52] Kim H, Arnoletti PJ, Christein J, et al. Pancreatic adenocarcinoma: a pilot study of quantitative perfusion and diffusion-weighted breath-hold magnetic resonance imaging. Abdom Imaging. 2014;39:744–752.
[53] Yao X, Zeng M, Wang H, et al. Evaluation of pancreatic cancer by multiple breath- hold dynamic contrast-enhanced magnetic resonance imaging at 3.0 T. Eur J Radiol. 2012;81:e917–e922.
[54] Kim JH, Lee JM, Park JH, et al. Solid pancreatic lesions: characterization by using timing bolus dynamic contrast-enhanced MR imaging assessment – a preliminary study. Radiology 2013;266: 185–196.